ACS APPLIED MATERIALS & INTERFACES

Research Article

www.acsami.org

# Effects of Cobalt Addition on the Catalytic Activity of the Ni-YSZ Anode Functional Layer and the Electrochemical Performance of Solid Oxide Fuel Cells

Ting Guo, Xiaolei Dong, Mandar M. Shirolkar, Xiao Song, Meng Wang, Lei Zhang, Ming Li, and Haiqian Wang*

Hefei National Laboratory for Physical Sciences at Microscale, University of Science and Technology of China, 96 Jinzhai Road, Hefei, Anhui 230026, P. R. China

Supporting Information

**ABSTRACT:** The effects of cobalt (Co) addition in the Ni-YSZ anode functional layer (AFL) on the structure and electrochemical performance of solid oxide fuel cells (SOFCs) are investigated. X-ray diffraction (XRD) analyses confirmed that the active metallic phase is a $Ni_{1-x}Co_x$ alloy under the operation conditions of the SOFC. Scanning electron microscopy (SEM) observations indicate that the grain size of $Ni_{1-x}Co_x$ increases with increasing Co content. Thermogravimetric analyses on the reduction of the $Ni_{1-x}Co_xO$-YSZ powders show that there are two processes: the chemical-reaction-controlled process and the diffusion-controlled process. It is found that the reduction peak corresponding to the chemical-reaction-controlled process in the DTG curves moves toward lower temperatures with increasing Co content, suggesting that the catalytic activity of $Ni_{1-x}Co_x$ is enhanced by the doping of Co. It is observed that the SOFC shows the best performance at $x = 0.03$, and the corresponding maximum power densities are 445, 651, and 815 mW $cm^{-2}$ at 700, 750, and 800 °C, respectively. The dependence of the SOFC performance on the Co content can be attributed to the competing results between the decreased three-phase-boundary length in the AFL and the enhanced catalytic activity of the $Ni_{1-x}Co_x$ phase with increasing Co content.

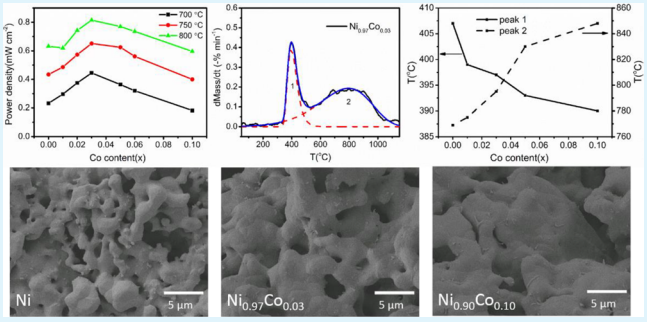


**KEYWORDS:** *nickel−cobalt alloy, catalytic, solid oxide fuel cells, anode functional layer, three-phase boundary, thermogravimetric analyses*

## 1. INTRODUCTION

Solid oxide fuel cells (SOFC) are electrochemical energy conversion devices that convert chemical energy in fuel directly into electricity without involving the process of combustion.[1,2] Nowadays, anode-supported SOFCs have been widely used because of their ease of fabrication, mechanical ruggedness, and high performance.[3−7] At the anode side of a SOFC, fuel is oxidized by the $O^{2-}$ migrated from the ionic conducting electrolyte with the help of the metallic catalytic phase along the three-phase boundary (TPB). Therefore, (1) inserting an anode functional layer (AFL) with fine microstructures to extend the TPB and (2) doping some transition metallic elements to improve the catalytic phase are important strategies for exploring high-performance SOFC anodes.[8−11]

Ni-YSZ cermet is one of the most widely used anode materials in SOFCs, which has been the subject of a number of research and development programs.[12,13] Up to now, cobalt (Co), with a character similar to that of nickel (Ni),[14] doping into Ni-containing SOFCs has already shown some benefits, such as enhancing the catalytic activity, reducing the carbon deposition, and improving the stability against $H_2S$.[15−22] For example, the results of Frade's group[19,23] show that the high-frequency resistance of the corresponding Ni−Co-YSZ cermet is smaller compared with that of samples without Co addition. Ishihara et al.[20] also reported that the performance of the cell was improved when Co was added into the Ni-YSZ anode. Grgicak et al. found that the Ni−Co-YSZ anode has better catalytic activity and stability than the Ni-YSZ anode when using CO- or $H_2S$-containing $H_2$ as a fuel.[21,22] Hyeon-Cheol et al. tried a variety of metal oxides and found that the addition of $Co_3O_4$ in the Ni-YSZ AFL is the most effective way toward improving the power density and reducing the area specific resistance of the cells.[24]

On the other hand, the active phase for catalyzing the fuel reaction at the anode side is the metallic grains (Ni grains in the Ni-YSZ anode, or $Ni_{1-x}Co_x$ grains in the Ni−Co-YSZ anode). However, such active metallic grains are in their oxide forms in the newly prepared single cells. They must undergo a reduction

Received: June 26, 2014
Accepted: August 27, 2014
Published: August 27, 2014

  

process at the first run of a SOFC operation. After reduction, the oxide grains are reduced to metallic ones. Understanding the reduction process may provide us valuable information about the electrochemical performances of the SOFC anode. The thermogravimetric (TG) measurement may be a useful way to analyze such reduction processes.[25−27]

In the present work, the effects of Co addition in the AFL on the electrochemical performance of LSM/YSZ/$Ni_{1-x}Co_x$-YSZ SOFCs and the reduction processes of the $Ni_{1-x}Co_xO$-YSZ anode materials are investigated. The microstructure evolution of $Ni_{1-x}Co_xO$ during reduction and the catalytic activity of the bimetallic $Ni_{1-x}Co_x$ phase are discussed.

## 2. EXPERIMENTAL SECTION

**2.1. Sample Preparation.** The $Ni_{1-x}Co_xO$-YSZ ($x$ = 0, 0.01, 0.03, 0.05, and 0.10) powders were prepared by mixing the appropriate amount of NiO (J.T. Baker, USA), $Co_3O_4$, and YSZ (TZ-8Y, Tosoh, Japan), where the weight ratio between NiO and YSZ is 55:45. $Co_3O_4$ was obtained by thermal decomposition of $Co(NO_3)_2{\cdot}6H_2O$ (Sinopharm Chemical Reagent Co., Ltd., China) at 350 °C for 2 h. After being ground for 30 min, the mixed powders were sintered at 1350 °C for 2 h in a muffle furnace.

The $Ni_{1-x}Co_x$-YSZ powders were obtained by reducing the $Ni_{1-x}Co_xO$-YSZ powders at 750 °C for 2 h in a ⌀ 32 mm × 500 mm tubular furnace with a constant $H_2$ flow rate of 40 sccm.

The single cells have a five-layered structure, and the typical microstructure is shown in Figure 1. The five layers are the Ni-YSZ

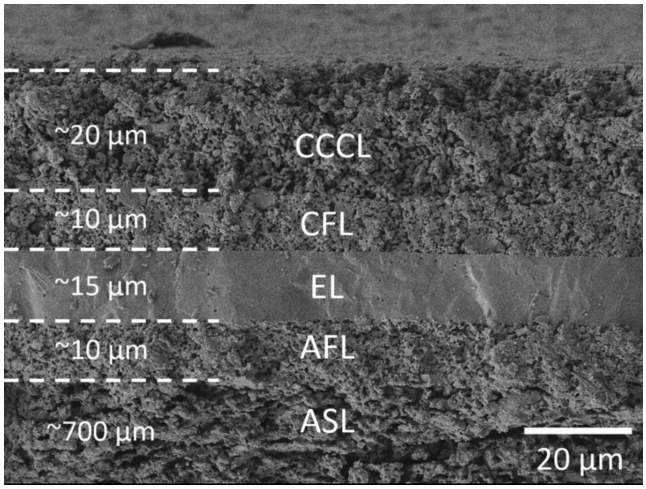


**Figure 1.** Cross-sectional SEM micrographs of a typical single cell after testing.

anode support layer (ASL), the $Ni_{1-x}Co_x$-YSZ ($x$ = 0, 0.01, 0.02, 0.03, 0.05, 0.06, and 0.10) AFL, the electrolyte layer (EL), the LSM-YSZ composite cathode functional layer (CFL), and the LSM cathode current collecting layer (CCCL), with thicknesses of about 700, 10, 15, 10, and 20 $\mu$m, respectively. We can see that the AFL and CFL are constructed with fine particles, while the ASL and CCCL are built with coarse particles. These kinds of anode-supported SOFCs have long TPB lengths and are favorable for gas diffusion at the same time. Meanwhile, the thickness of the EL stays in a suitable range, which ensures both a good mechanical property and a relatively low resistance. The EL and AFL were prepared by a wet powder spraying method: suspensions of corresponding powders and a proper amount of organic additives were mixed and sprayed on the substrate, respectively. The ASL was prepared by tape-casting the corresponding slurry on the AFL. The half-cells were sintered at 1350 °C for 2 h. The CFL and CCCL were screen-printed onto the half-cells subsequently and then cosintered at 1125 °C for 3 h. The active area of the single cells is 2 × 2 $cm^2$. Details for preparation of the cells can be found in our previous report.[28]

**2.2. Measurement.** The phase of the $Ni_{1-x}Co_x$-YSZ powders was evaluated by X-ray diffraction (XRD; MXPAHF, MacScience) with Cu K$\alpha$ radiation over the range of $2\theta$ = 20−80° at room temperature. The microstructure of the samples was observed by scanning electron microscopy (SEM; JSM6700, JEOL). The TG measurements of the $Ni_{1-x}Co_xO$-YSZ powders were taken by a simultaneous thermal analyzer (STA449F3, NETZSCH). The samples were reduced in a $H_2$ (10 vol %)/$N_2$ (90 vol %) atmosphere with a flow rate of 60 mL $min^{-1}$ at a heating rate of 10 °C $min^{-1}$ up to 1200 °C.

The single-cell performances were evaluated by a direct-current electronic load (N3300, Agilent) from 700 to 800 °C using the two-electrode and four-wire setup with 300 sccm humidified $H_2$ (2−3% $H_2O$) as the fuel and air as the oxidant. The electrochemical impedance spectra of single cells were measured in an open-circuit voltage (OCV) condition by an electrochemical workstation (IM6eX, Zahner) in a frequency range of 0.05−$10^5$ Hz with an alternating-current signal amplitude of 20 mV. The anodes were reduced in situ at 750 °C.

## 3. RESULTS AND DISCUSSION

**3.1. XRD Analysis.** Figure 2a shows the XRD patterns of the $Ni_{1-x}Co_xO$-YSZ powders, which are sintered at 1350 °C for

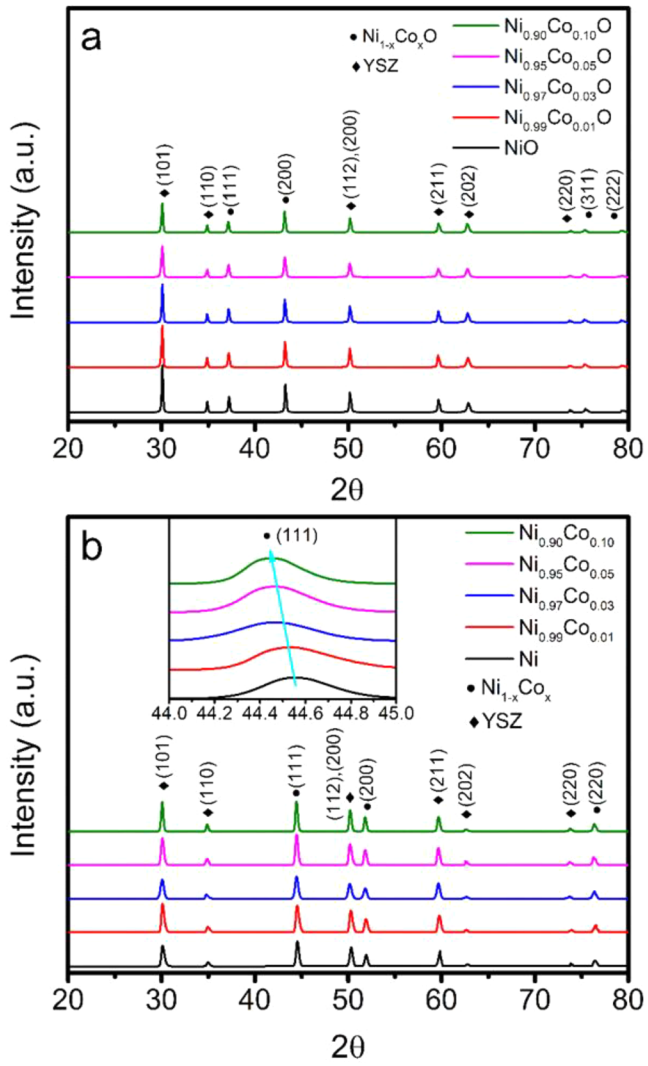


**Figure 2.** XRD patterns of (a) $Ni_{1-x}Co_xO$-YSZ and (b) $Ni_{1-x}Co_x$-YSZ powders with different Co contents.

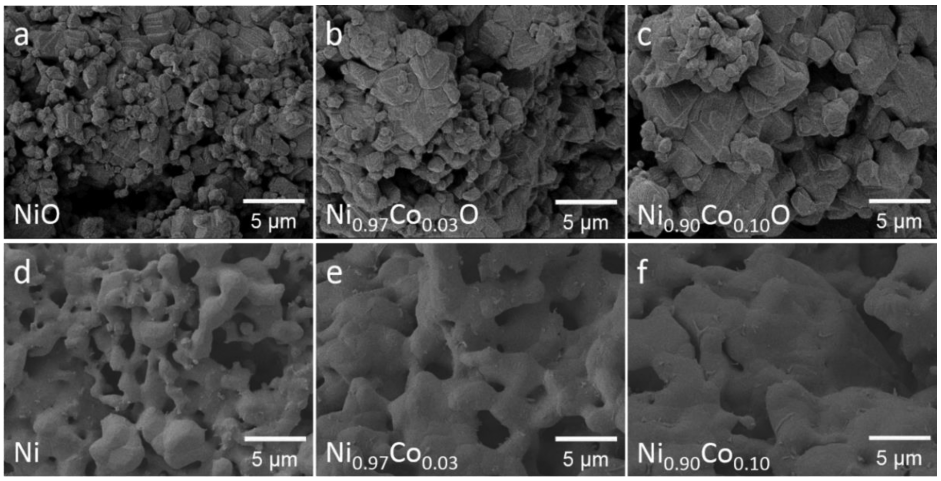


**Figure 3.** SEM images of $Ni_{1-x}Co_xO$ particles with $x$ = (a) 0, (b) 0.03, and (c) 0.10 before reduction and of $Ni_{1-x}Co_x$ particles with $x$ = (d) 0, (e) 0.03, and (f) 0.10 after reduction.

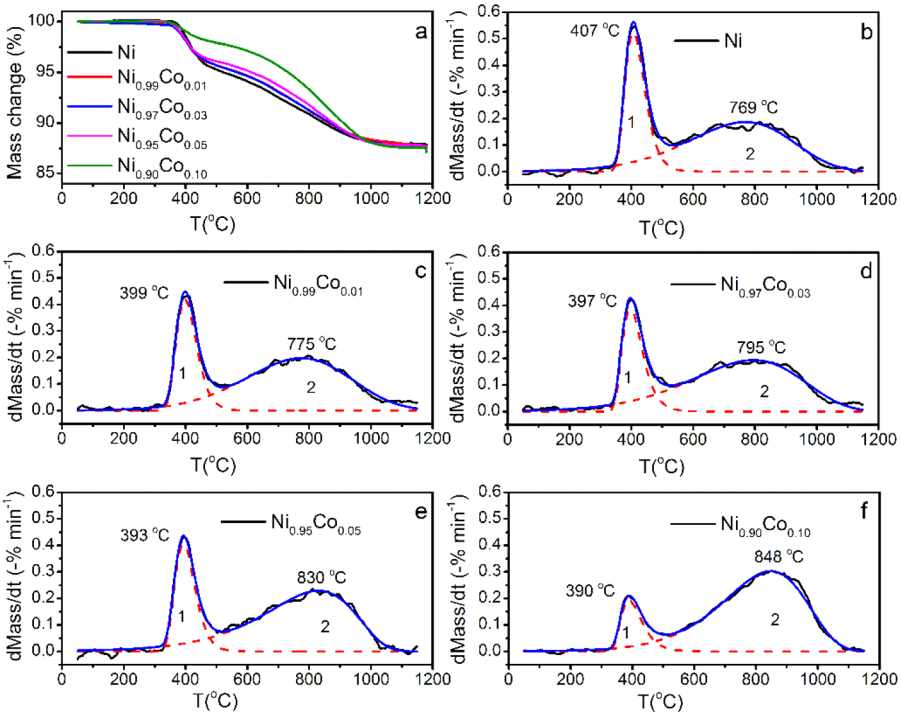


**Figure 4.** (a) TG curves and (b–f) DTG curves of different $Ni_{1-x}Co_xO$-YSZ powders in $H_2$ (10 vol %)/$N_2$ (90 vol %) atmospheres with a constant heating rate.

2 h. NiO and YSZ related peaks are observed without the presence of either the CoO or $Co_3O_4$ phase, which suggests that Co atoms are incorporated into the NiO lattice and a $Ni_{1-x}Co_xO$ solid solution is formed. This phenomenon is also reported in other literature.[29,30]

Figure 2b shows the XRD patterns of the $Ni_{1-x}Co_x$-YSZ powders used in the AFL, which were obtained by reducing the $Ni_{1-x}Co_xO$-YSZ powders in $H_2$ at 750 °C. The crystal structure of metallic Ni is face-centered-cubic (FCC), while that for metallic Co is hexagonal-close-packed.[31] Only peaks belonging to YSZ and the Ni FCC crystal structure are observed. The inset of Figure 2b illustrates the main diffraction peak of Ni(111) with different Co contents. It is seen that the Ni(111) peak shifts from $2\theta$ = 44.54° to 44.45° as $x$ increases from 0 to 0.10, indicating that the lattice parameter increases by the doping of Co. The other diffraction peaks [the Ni(200) and Ni(220) peaks] also shift to lower angles, correspondingly. It is known that the atomic radius of Co (1.26 Å) is larger than that of Ni (1.24 Å), so the increase in the lattice parameter indicates that the Co atoms are effectively incorporated into the Ni lattice, and the $Ni_{1-x}Co_x$ alloy is formed. No obvious changes were observed for YSZ peaks, suggesting that Co addition does not change the crystalline structure of YSZ. Compared with Figure 2a, no obvious changes were observed for YSZ after reduction, suggesting that YSZ is stable in the reducing atmosphere.

**3.2. SEM Analysis of the $Ni_{1-x}Co_x$ and $Ni_{1-x}Co_xO$ Powders.** The SEM images of the $Ni_{1-x}Co_xO$ particles before and after reduction are shown in Figure 3. The $Ni_{1-x}Co_xO$ powders used here were prepared by using the same method as


dx.doi.org/10.1021/am504148m | ACS Appl. Mater. Interfaces 2014, 6, 16131–16139

that of the $Ni_{1-x}Co_xO$-YSZ powders used for the AFL. The primary reasons to use $Ni_{1-x}Co_xO$ powders instead of $Ni_{1-x}Co_xO$-YSZ powders are as follows: (1) our main concern is to observe the morphology evolution of the active catalytic phase in the AFL, and (2) when we use $Ni_{1-x}Co_xO$-YSZ powders, the reduced $Ni_{1-x}Co_x$ grains cannot be well-resolved because they are buried in the YSZ matrix. Although the absence of a YSZ matrix may favor the long-distance migration of the metallic elements and result in larger $Ni_{1-x}Co_x$ grains, the basic trend of the morphology evolution during reduction should stay the same. It can be seen from Figure 3 that, before reduction, the grain size of $Ni_{1-x}Co_xO$ grows as the Co content increases, which can be attributed to the fact that Co addition promotes the sintering behavior of $Ni_{1-x}Co_xO$.[30] After reduction at a high temperature (750 °C), the $Ni_{1-x}Co_x$ grains tend to aggregate into a porous structure. It is more interesting to see that, as $x$ increases, the number of pores decreases and the $Ni_{1-x}Co_x$ grains become larger. The formation of the porous structure can be easily understood by considering volume contraction of the $Ni_{1-x}Co_xO$ grains in the reduction process. The larger grains of $Ni_{1-x}Co_x$ with higher Co content may be inherited from the corresponding oxide powders. Moreover, the reduction process was performed at high temperature, so a sintering process is taking place simultaneously.[12,32,33] It should be mentioned here that, in the reduction process, the lattice of the oxide collapses by removing O, and the Ni (and Co) atoms will renucleate and grow to form new crystalline grains. Therefore, the growth of the Ni grains in the reduction process is much faster than that happening in a SOFC anode under normal operating conditions. It is known that the $Ni_{1-x}Co_x$ alloy has a lower melting point than Ni. Therefore, the $Ni_{1-x}Co_x$ grains tend to grow larger as the Co content increases.

**3.3. TG Analyses.** Figure 4a shows the TG curves corresponding to the reduction processes of different $Ni_{1-x}Co_x$-YSZ powders in a $H_2$ (10 vol %)/$N_2$ (90 vol %) atmosphere with a constant heating rate of 10 °C $min^{-1}$. At 1100 °C, the mass loss of the samples is around 12%, which is very close to the theoretical values (the theoretical mass loss for the samples ranges from 11.8% to 12.6% as $x$ increases from 0 to 0.10), indicating that $Ni_{1-x}Co_xO$ is completely reduced to the $Ni_{1-x}Co_x$ alloy. Parts b–f of Figure 4 show the differential thermogravimetric (DTG) curves of different $Ni_{1-x}Co_xO$-YSZ powders based in Figure 4a. It is seen that there are two peaks, a narrow low-temperature peak (peak 1) and a broad high-temperature peak (peak 2), for each sample. All of these DTG curves can be well fitted with two overlapped Fraser–Suzuki functions,[34,35] as illustrated by the dashed lines in Figure 4b–f. This suggests that there are two well-defined reaction kinetics corresponding to the reduction process. Apparently, YSZ is very stable in the reducing environment. Therefore, all of the weight losses in the DTG study come from the reduction processes of the $Ni_{1-x}Co_xO$ powders.

The shrinkage-core model is one of the prevailing models for NiO reduction.[36−38] The simple shrinkage-core model assumes that the NiO grain or particle is nonporous, and the Ni–NiO interface moves toward the center of the particles, leaving behind a metallic product layer during reduction. Szekely et al.[36] modified the simple shrinkage-core model: they suggest that NiO particles or pellets are porous agglomerations of NiO grains and each grain undergoes a microscopic shrinking-core process during reduction. In this modified shrinkage-core model, there are two main kinetics during the reduction:[36,39] a chemical-reaction-controlled process and a diffusion-controlled process. In the chemical-reaction-controlled process, the reaction rate is determined by the reduction process happening at the surface of the NiO grains. In the diffusion-controlled process, the reaction rate is determined by the diffusion process of $H_2$ through the pores between the NiO particles and through the Ni product layer. Kim et al.[25] studied the reduction process of NiO by TG analyses with simultaneous monitoring of the relative humidity of the outlet gas and suggest that water vapor also plays an important part in the diffusion-controlled process. Szekely et al. also suggest that, during the reduction process of NiO particles, the chemical-reaction-controlled process dominates at low temperatures, while the diffusion-controlled process dominates in high-temperature toward the end of the reaction. Lee et al.[40] also observed two DTG peaks in the reduction process of nanoagglomerate NiO powders. They attributed the low-temperature sharp and narrow peaks to the chemical-reaction-controlled process and the high-temperature wide peak to the diffusion-controlled process.

The positions of peaks 1 and 2 with different Co contents are shown in Figure 5. It is observed that the position of peak 1

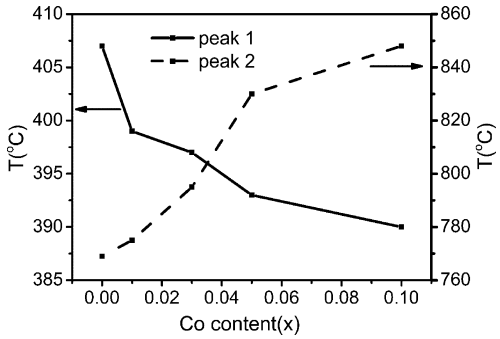


**Figure 5.** Peak positions of peaks 1 and 2 with different Co contents obtained from Figure 4b–f.

decreases from 407 to 390 °C as $x$ increases from 0 to 0.10. The overall reduction process of $Ni_{1-x}Co_xO$ follows:

$$Ni_{1-x}Co_xO + H_2 \rightarrow Ni_{1-x}Co_x + H_2O(gas) \quad (1)$$

This is an autocatalytic reaction. It starts with an induction period in which $H_2$ is slowly dissociated by NiO. After this induction period, $H_2$ dissociates rapidly by the preformed Ni metal catalyst.[38,41] As discussed above, peak 1 is dominated by the chemical reaction process at the surface of the $Ni_{1-x}Co_xO$ grains; therefore, the shift of peak 1 toward a lower temperature range indicates that the doping of Co may promote reaction (1) at low temperature; namely, Co doping reduces the activation energy of the reaction.

The activation energy of reaction (1) may be influenced by the grain size or the intrinsic chemical properties of $Ni_{1-x}Co_xO$ (and $Ni_{1-x}Co_x$ if we consider the autocatalytic effect). Apparently, the grain size effect cannot explain the shift of peak 1. It is known that smaller grains have lower activation energies. However, from Figure 3, we can see that both the grain sizes of $Ni_{1-x}Co_xO$ and $Ni_{1-x}Co_x$ increase with $x$. This grain size change shows a trend opposite to that of the activation energy, which decreases with increasing Co content. Moreover, all of the samples used in our TG analysis were carefully prepared to avoid the grain size effect. By mixing YSZ with $Ni_{1-x}Co_xO$ and sintering at 1350 °C, YSZ forms an almost identical cage-structured matrix, in which the $Ni_{1-x}Co_xO$ grains

are embedded. The constrained sintering of the $Ni_{1-x}Co_xO$ grains in the YSZ matrix makes the $Ni_{1-x}Co_xO$ grain size very uniform. Our SEM analyses (see the Supporting Information) indicate that the typical grain sizes of the powders used for the TG measurements are about 1−3 $\mu$m, regardless of the Co content. Through exclusion of the grain size effect, the shift of peak 1 can only be attributed to the changes in the intrinsic chemical properties of $Ni_{1-x}Co_xO$ and $Ni_{1-x}Co_x$. That means, the doping of Co increases the reactivity of $Ni_{1-x}Co_xO$ and $Ni_{1-x}Co_x$ with $H_2$ or, equivalently, reduces the activation energy of reaction (1).

Reaction (1) is a surface reaction between the $H_2$ molecules and the solid surface of $Ni_{1-x}Co_xO$ and $Ni_{1-x}Co_x$. Such a kind of surface reaction depends on the electronic states of the solid surface.[42] When Co is doped, the surface electronic states of $Ni_{1-x}Co_xO$ and $Ni_{1-x}Co_x$ will be changed, thus resulting in changes in the activation energy of reaction (1). Considering the autocatalytic effect, we think that the metallic phase $Ni_{1-x}Co_x$ should be the dominate factor for the activation energy of reaction (1). However, the detailed mechanism remains an open question.

The position of peak 2 in Figure 5 shows a changing trend opposite to that of peak 1; it shifts to a higher temperature from 769 to 848 °C as the Co content increases. As discussed before, peak 2 is dominated by the diffusion-controlled process. During the reduction process, the surface part of the $Ni_{1-x}Co_xO$ grains is first reduced to small metallic $Ni_{1-x}Co_x$ grains. These grains cover the surface of the unreduced NiCoO grains in the form of a thin layer, which will slow down the gas diffusion rate. Therefore, the diffusion process may be influenced by two factors: the porosity of the aggregated $Ni_{1-x}Co_x$ grains and the coverage of the preformed $Ni_{1-x}Co_x$ metallic layer on the $Ni_{1-x}Co_xO$ grains. From Figure 3, we can see that the porosity of the $Ni_{1-x}Co_x$ particles decreases as $x$ increases, and the decreased porosity will slow down the gas ($H_2$ or $H_2O$) diffusion rate. Moreover, the incorporation of Co into Ni may also favor the formation of a thin and dense metallic layer (shell) on the unreduced $Ni_{1-x}Co_xO$ core, either by reducing the surface energy of the metallic shell or by increasing the affinity between the shell and core. A thin but dense metallic layer will also slow down the gas diffusion rate. The lowered diffusion rate as a result of structural reasons (low porosity and high coverage of metallic layer) can be compensated for by a higher temperature. Therefore, the position of peak 2 shifts to higher temperature as the Co content increases.

The peak area ratio (AP1/AP2, where AP1 and AP2 are the areas of peaks 1 and 2, respectively) calculated from Figure 4b−f is shown in Figure 6. AP1/AP2 shows a decreasing trend with increasing Co content. AP1/AP2 reflects the ratio of weight loss from the chemical-reaction-controlled process to that from the diffusion-controlled process. The smaller the value of AP1/AP2, the less preformed metallic layer is needed to cover the unreduced $Ni_{1-x}Co_xO$ grains, which means that the process switches from the chemical-reaction-controlled process to the diffusion-controlled process earlier. Therefore, the result of Figure 6 also supports the above discussions: the doping of Co may promote the formation of a thin and less porous metallic layer, which will slow down the gas diffusion rate.

**3.4. SOFC Tests.** Parts a−c of Figure 7 show the typical V−I performances of the cells with different Co contents at 700, 750, and 800 °C. The maximal power density corresponding to different Co contents is shown in Figure 7d. It is observed that there is an optimal Co content at $x$ = 0.03, according to the highest maximal power density. At 700, 750, and 800 °C, the maximal power densities corresponding to the optimal sample reach 445, 651, and 815 mW cm$^{-2}$ respectively, that is, 92%, 50%, and 29% higher than those of the sample without Co (232, 434, and 632 mW cm$^{-2}$).

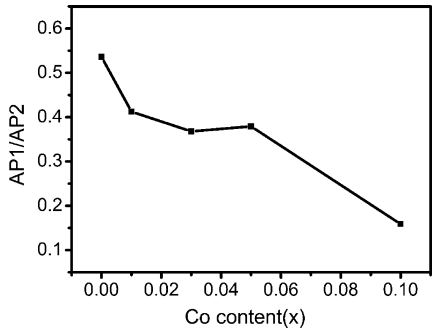


**Figure 6.** AP1/AP2 with different Co contents calculated from Figure 4b−f.

Figure 8a shows the measured impedance spectra of the cells with different Co contents at 700, 750, and 800 °C under OCV. Under the OCV condition, the polarization resistance is mainly contributed by the activation polarization resistance of the cell.[43] It is seen that the arcs vary with the Co content obviously at different temperatures, indicating that the doping of Co in the AFL has important influences on the polarization resistance of the cells. As we know, the ohmic resistance ($R_0$) of the cell mainly comes from the ionic resistance of the electrolyte, the electronic resistance of the electrodes, and the resistance from the leads of the external circuit. The value and variation of $R_0$ are small compared to those of the polarization resistance, and $R_0$ does not affect the polarization processes of the cells, so it will not be discussed further.

Equivalent circuit modeling has been proven to be a useful tool for analyzing the impedance spectra.[44] Through application of an equivalent circuit model, the resistance of a cell can be roughly divided into three parts: the ohmic resistance ($R_0$), the anodic polarization resistance ($R_A$), and the cathodic polarization resistance ($R_C$). Furthermore, in each of the electrodes (anode or cathode), two processes may contribute to the polarization resistance: a charge-transfer process (corresponding to the electrode reaction, for example, the formation of $H_2O$ at the anode side), the responses of which are at high frequency range, and a mass-transfer process (corresponding to the dissociative adsorption and the surface diffusion/gas-phase diffusion process), the responses of which are at low frequency range.[45] Therefore, we use a four-element ($RQ$) equivalent circuit model to simulate the polarization resistance of the cells, as illustrated in Figure 8b. Four- or five-element equivalent circuit models have also been used by many other authors.[46,47] Here, $R$ represents for the resistance, $Q$ for the constant phase element, the subscripts A and C stand for the anode and cathode, and the subscripts H and L are for the high- and low-frequency responses, respectively. In order to exclude the influences from the external circuit, an inductor $L_0$ is also introduced in the simulation but subtracted from the results.[46,48] The lower part of Figure 8b shows the fitting result of the sample with a Co content of $x$ = 0.03 in the AFL at 750 °C. The relaxation frequencies of the anode processes $P_{AH}$ and $P_{AL}$ are around 10 kHz and 10 Hz, while those of $P_{CH}$ and $P_{CL}$ are around 1 kHz and 0.5 Hz, respectively. The frequency

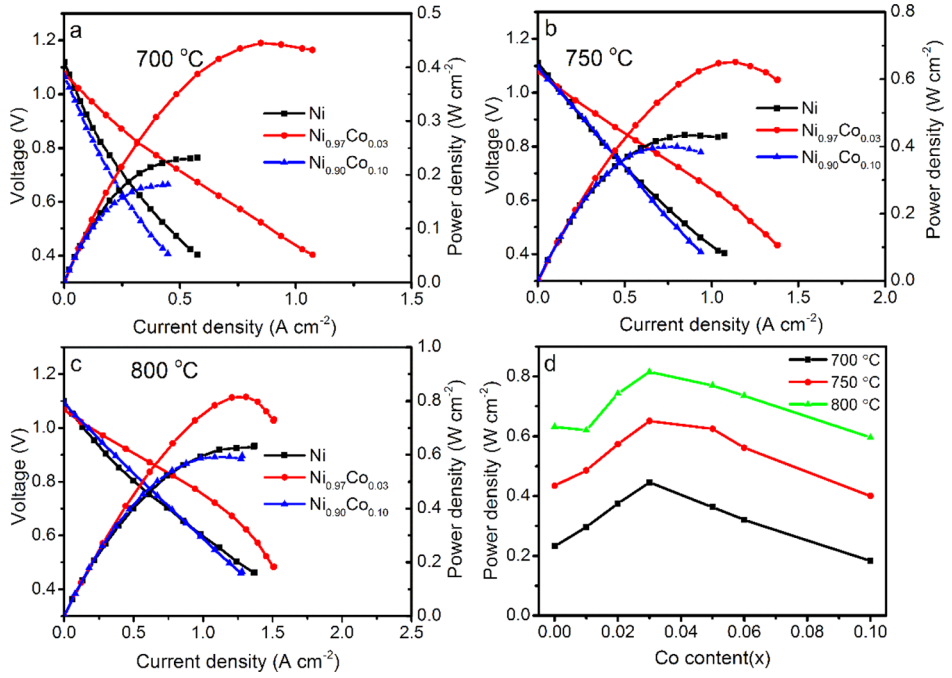


**Figure 7.** V–I performance of cells with different Co contents at (a) 700 °C, (b) 750 °C, and (c) 800 °C and (d) maximal power density of different Co contents at different temperatures.

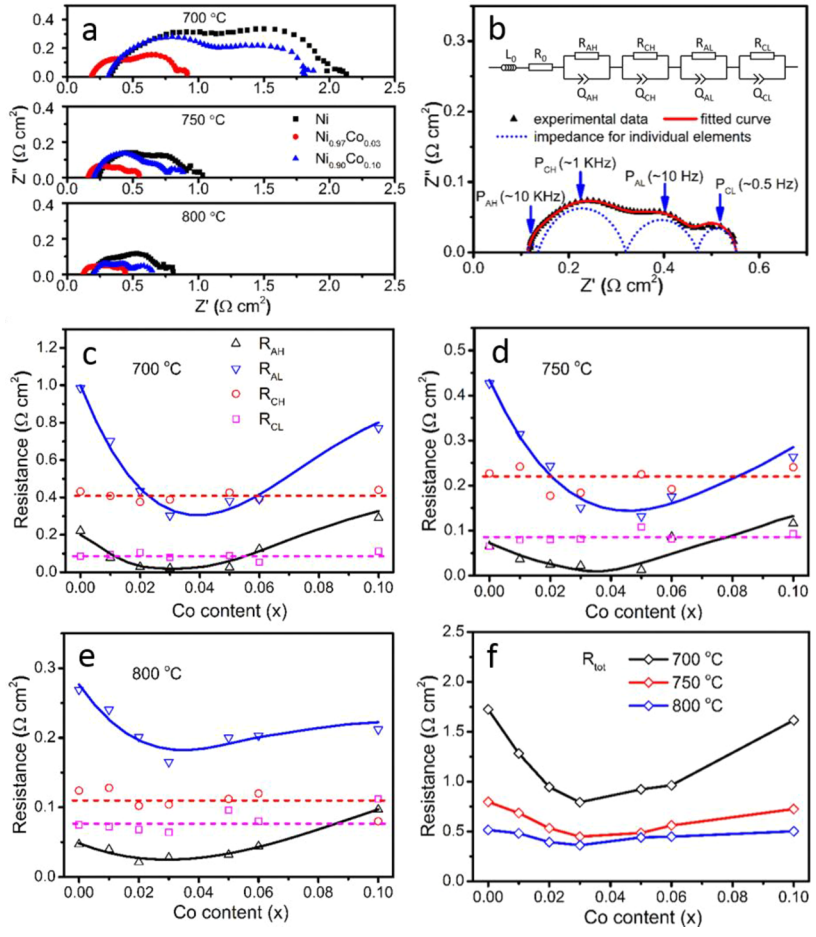


**Figure 8.** (a) Impedance of the cells with different Co contents at 700, 750, and 800 °C under OCV. (b) Fitting result of the cell with a Co content of $x = 0.03$ in the AFL at 750 °C. Analyzed polarization resistance of $R_{AH}$, $R_{AL}$, $R_{CH}$, and $R_{CL}$ at (c) 700, (d) 750, and (e) 800 °C for the samples with different Co contents. (f) Total polarization resistance for different samples at 700, 750, and 800 °C.

responses of all samples are comparable with the reported data,[46,49,50] indicating that our simulation is reasonable.

The simulated polarization resistances $R_{AH}$, $R_{AL}$, $R_{CH}$, and $R_{CL}$ at different temperatures are shown in Figure 8c−e. It is observed that $R_{AL}$ and $R_{AH}$ show obvious variations with the Co content and have minimum values at around $x = 0.03$. On the contrary, $R_{CL}$ and $R_{CH}$ remain almost unchanged with different Co contents, indicating that Co doping in the AFL does not affect the polarization of the cathode. In the preparation process of the single cells, all of the parameters and conditions are the same, except the Co content in the AFL, so the changes in $R_{AL}$ and $R_{AH}$ should originate from the AFL. It is also seen that $R_{AL}$ is much higher than $R_{AH}$, indicating that the mass-transfer effect should be dominant in the anodic processes. Considering that the impedance spectra were measured under OCV condition, the $H_2$ and $H_2O$ gas diffusion through the pores in the anode should be insignificant. Therefore, the mass-transfer processes corresponding to the dissociative adsorption and surface diffusion in the anodic TPB region should be the dominant factors. Mizusaki and coauthors[51] also suggested a rate-determining step of dissociative adsorption or surface diffusion on the Ni surface by taking into account the role of TPB. The small but clear variation in $R_{AH}$ indicates that the charge-transfer process in the AFL is also affected by the doping of Co.

Figure 8f shows the total polarization resistance ($R_{tot}$, the sum of $R_{AL}$, $R_{AH}$, $R_{CL}$, and $R_{CH}$) with different Co contents. $R_{tot}$ presents a minimum value at about $x = 0.03$. According to the above discussions, the change in $R_{tot}$ is mainly attributed to $R_{AH}$ and $R_{AL}$. At 700, 750, and 800 °C, the minimum total polarization resistances are 0.792, 0.438, and 0.361 Ω cm$^2$, respectively, which is 54%, 44%, and 30% lower than those of the sample without Co (1.724, 0.785, and 0.515 Ω cm$^2$). This indicates that a proper amount of Co doping in the Ni-YSZ AFL will reduce the polarization resistance of the single cells by enhancing the mass- and charge-transfer processes in the anode. Moreover, the changing tendency in the cell performance (see Figure 7d) well matches that of $R_{tot}$, indicating that the cell with lower polarization resistance has better performance.[52]

**3.5. Effects of the Co Addition in the AFL on the Performance of SOFC.** It is interesting to correlate the performance of the SOFC anode with the results of TG analyses. In fact, there are many similarities between the SOFC anode reaction and the reduction of $Ni_{1-x}Co_xO$. At the anode side of the SOFC, $H_2$ reacts with $O^{2-}$ ions migrated from the ionic conducting electrolyte with the help of the metallic catalytic phase ($Ni_{1-x}Co_x$) along the three-phase boundaries.[53] In the reduction process of $Ni_{1-x}Co_xO$, $H_2$ reacts with $O^{2-}$ ions residing at the surface of the $Ni_{1-x}Co_xO$ and autocatalyzed by the preformed $Ni_{1-x}Co_x$. More specifically, both of the reaction processes involve similar elementary reaction steps: (1) dissociation of $H_2$, (2) surface diffusion of H atoms to a reactive center, and (3) rupture of Ni−O bonds. These elementary reactions can be written in the Kröger−Vink notation as[54,55]

$$H_2(gas) + 2[]_M \leftrightarrow 2H_M \quad (2)$$

$$H_M + O_M \leftrightarrow OH_M + []_M \quad (3)$$

$$OH_M + H_M \leftrightarrow H_2O_M + []_M \quad (4)$$

where M denotes the $Ni_{1-x}Co_x$ alloy and $[]_M$ denotes a free surface site at the M surface. Therefore, the $Ni_{1-x}Co_x$ phase should play a similar role in catalyzing both the SOFC reaction and $Ni_{1-x}Co_xO$ reduction processes. On the basis of the above impedance analyses of SOFC single cells, the dissociative adsorption and surface diffusion of hydrogen should be the dominant factors in the catalysis processes.

As discussed in the TG analyses section (section 3.3), peak 1 in the DTG curves reflects the chemical-reaction-controlled process of the surface reaction (1), and the doping of Co into Ni can reduce the activation energy of the $Ni_{1-x}Co_xO$ reduction. On the other hand, the SOFC test results indicate that the polarization resistance decreases and the performance of the cell improves with the increasing content of Co in the AFL until $x$ reaches 0.03 (see Figures 7 and 8). Because all of the cells are prepared with the same design and method, except that the Co content is different in the AFL, we think the improved performance of the cells can be attributed to the doping of Co, which increases the catalytic activity of Ni.

However, different from the monotonous changing trend of the peak 1 position with the Co content (see Figure 5), when $x$ increases to over 0.03, the performance of SOFC declines. This should be due to the microstructural reason. As we have seen in Figure 3, the microstructure of the porous aggregated $Ni_{1-x}Co_x$ grains becomes coarser at larger $x$. Coarse grains of the metallic phase will reduce the TPB length in the AFL region. As a result, the activation polarization resistance of the anode increases and the cell performance declines.[56−58]

In a number of instances, alloys have been shown to have superior catalytic properties compared with elementary metals.[59] In fact, the improvement of the SOFC performances by doping Co into the Ni-YSZ anode has been comprehensively reported.[19−21,24] However, most of the authors tend to attribute the enhanced performance of SOFC either to the increase in the TPB length or to the specific surface area in the anode. Although some of the authors think that there should be a synergistic effect between Co and Ni, leading to an enhanced catalytic activity that is better than pure Ni or Co,[21] there is still a lack of evidence from experiments. By correlating the results from TG analyses, we proved that the enhanced performance of SOFC should originate from the synergistic effect of the $Ni_{1-x}Co_x$ bimetallic catalytic material. This method can also be used to explore other catalytic materials.

## 4. CONCLUSION

In the present work, the effects of Co addition in the Ni-YSZ AFL on the structure and electrochemical performance of SOFC are investigated. XRD analyses confirmed that the active metallic phase is a $Ni_{1-x}Co_x$ alloy under the operation conditions of the SOFC. SEM observations indicate that the grain size of $Ni_{1-x}Co_x$ increases with an increase in $x$. TG analyses about the reduction of the $Ni_{1-x}Co_xO$-YSZ powders show that there are two processes: the first is a chemical-reaction-controlled surface process, and the second is a gas-diffusion-controlled process. It is found that the reduction peak corresponding to the chemical-reaction-controlled surface process in the DTG curves moves toward lower temperatures with an increase of the Co content, which suggests that the catalytic activity of $Ni_{1-x}Co_x$ is enhanced by the doping of Co.

On the other hand, the best performance of the SOFC is observed at $x = 0.03$, and the maximum power densities are 445, 651, and 815 mW cm$^{-2}$ at 700, 750, and 800 °C, respectively. The dependence of the SOFC performance on the

Co content can be attributed to the competing results of the decreased TPB length in the AFL and the enhanced catalytic activity of the $Ni_{1-x}Co_x$ phase with increasing Co content.

## ■ ASSOCIATED CONTENT

### Supporting Information

SEM images of different $Ni_{1-x}Co_xO$-YSZ powders used for the TG measurements. This material is available free of charge via the Internet at http://pubs.acs.org.

## ■ AUTHOR INFORMATION


### Corresponding Author

*Tel.: +86 551 63603770. Fax: +86 551 63606266. E-mail: hqwang@ustc.edu.cn.


### Author Contributions

The manuscript was written through contributions of all authors. All authors have given approval to the final version of the manuscript.

### Notes

The authors declare no competing financial interest.

## ■ ABBREVIATIONS

ASL, anode support layer; AFL, anode functional layer; EL, electrolyte layer; CFL, cathode functional layer; CCCL, cathode current collecting layer; TPB, three-phase boundary; OCV, open-circuit voltage

## ■ REFERENCES


(1) Ormerod, R. M. Solid Oxide Fuel Cells. *Chem. Soc. Rev.* **2003**, *32*, 17−28.

(2) Guo, T.; Zhang, L.; Song, X.; Dong, X.; Shirolkar, M. M.; Wang, M.; Li, M.; Wang, H. Influences of $Gd_2Ti_2O_7$ Sintering Aid on the Densification, Ionic Conductivity and Thermal Expansion of $Gd_{0.1}Ce_{0.9}O_{1.95}$ Electrolyte for Solid Oxide Fuel Cells. *J. Power Sources* **2014**, *262*, 239−244.

(3) Zhao, F.; Virkar, A. V. Dependence of Polarization in Anode-Supported Solid Oxide Fuel Cells on Various Cell Parameters. *J. Power Sources* **2005**, *141*, 79−95.

(4) Park, H. C.; Virkar, A. V. Bimetallic (Ni−Fe) Anode-Supported Solid Oxide Fuel Cells with Gadolinia-Doped Ceria Electrolyte. *J. Power Sources* **2009**, *186*, 133−137.

(5) Virkar, A. V.; Chen, J.; Tanner, C. W.; Kim, J. W. The Role of Electrode Microstructure on Activation and Concentration Polarizations in Solid Oxide Fuel Cells. *Solid State Ionics* **2000**, *131*, 189−198.

(6) Chen, K. F.; Chen, X. J.; Lu, Z.; Ai, N.; Huang, X. Q.; Su, W. H. Performance of an Anode-Supported SOFC with Anode Functional Layers. *Electrochim. Acta* **2008**, *53*, 7825−7830.

(7) Chen, Y.; Zhang, Y. X.; Baker, J.; Majumdar, P.; Yang, Z. B.; Han, M. F.; Chen, F. L. Hierarchically Oriented Macroporous Anode-Supported Solid Oxide Fuel Cell with Thin Ceria Electrolyte Film. *ACS Appl. Mater. Interfaces* **2014**, *6*, 5130−5136.

(8) Kan, H.; Lee, H. Sn-Doped Ni/YSZ Anode Catalysts with Enhanced Carbon Deposition Resistance for an Intermediate Temperature SOFC. *Appl. Catal., B* **2010**, *97*, 108−114.

(9) Wang, Z. H.; Zhang, N. Q.; Qiao, J. S.; Sun, K. N.; Xu, P. Improved SOFC Performance with Continuously Graded Anode Functional Layer. *Electrochem. Commun.* **2009**, *11*, 1120−1123.

(10) Gross, M. D.; Vohs, J. M.; Gorte, R. J. An Examination of SOFC Anode Functional Layers Based on Ceria in YSZ. *J. Electrochem. Soc.* **2007**, *154*, B694−B699.

(11) Marina, O. A.; Bagger, C.; Primdahl, S.; Mogensen, M.; Solid Oxide, A. Fuel Cell with a Gadolinia-Doped Ceria Anode: Preparation and Performance. *Solid State Ionics* **1999**, *123*, 199−208.

(12) Jiang, S. P.; Chan, S. H. A Review of Anode Materials Development in Solid Oxide Fuel Cells. *J. Mater. Sci.* **2004**, *39*, 4405−4439.

(13) Cowin, P. I.; Petit, C. T. G.; Lan, R.; Irvine, J. T. S.; Tao, S. W. Recent Progress in the Development of Anode Materials for Solid Oxide Fuel Cells. *Adv. Energy Mater.* **2011**, *1*, 314−332.

(14) Minh, N. Q. Ceramic Fuel-Cells. *J. Am. Ceram. Soc.* **1993**, *76*, 563−588.

(15) Benyoucef, A.; Klein, D.; Coddet, C.; Benyoucef, B. Development and Characterisation of (Ni, Cu, Co)-YSZ and Cu−Co-YSZ Cermets Anode Materials for SOFC Application. *Surf. Coat. Technol.* **2008**, *202*, 2202−2207.

(16) Ringuede, A.; Labrincha, J. A.; Frade, J. R. A Combustion Synthesis Method to Obtain Alternative Cermet Materials for SOFC Anodes. *Solid State Ionics* **2001**, *141*, 549−557.

(17) O'Brien, J. S.; Giorgi, J. B. Solid Oxide Fuel Cell with NiCo-YSZ Cermet Anode for Oxidation of $CO/H_2$ Fuel Mixtures. *J. Power Sources* **2012**, *200*, 14−20.

(18) Resini, C.; Delgado, M. C. H.; Presto, S.; Alemany, L. J.; Riani, P.; Marazza, R.; Ramis, G.; Busca, G. Yttria-Stabilized Zirconia (YSZ) Supported Ni−Co Alloys (Precursor of SOFC Anodes) as Catalysts for the Steam Reforming of Ethanol. *Int. J. Hydrogen Energy* **2008**, *33*, 3728−3735.

(19) Ringuede, A.; Fagg, D. P.; Frade, J. R. Electrochemical Behaviour and Degradation of (Ni,M)/YSZ Cermet Electrodes (M = Co,Cu,Fe) for High Temperature Applications of Solid Electrolytes. *J. Eur. Ceram. Soc.* **2004**, *24*, 1355−1358.

(20) Ishihara, T.; Yan, J. W.; Shinagawa, M.; Matsumoto, H. Ni−Fe Bimetallic Anode as an Active Anode for Intermediate Temperature SOFC Using $LaGaO_3$ Based Electrolyte Film. *Electrochim. Acta* **2006**, *52*, 1645−1650.

(21) Grgicak, C. M.; Pakulska, M. M.; O'Brien, J. S.; Giorgi, J. B. Synergistic Effects of Ni(1−*x*)Co(*x*)-YSZ and Ni(1−*x*)Cu(*x*)-YSZ Alloyed Cermet SOFC Anodes for Oxidation of Hydrogen and Methane Fuels Containing H(2)S. *J. Power Sources* **2008**, *183*, 26−33.

(22) Grgicak, C. M.; Giorgi, J. B. Improved Performance of Ni- and Co-YSZ Anodes via Sulfidation to NiS- and CoS-YSZ. Effects of Temperature on Electrokinetic Parameters. *J. Phys. Chem. C* **2007**, *111*, 15446−15455.

(23) Ringuede, A.; Bronine, D.; Frade, J. R. $Ni_{1-x}Co_x$/YSZ Cermet Anodes for Solid Oxide Fuel Cells. *Electrochim. Acta* **2002**, *48*, 437−442.

(24) Park, H. C.; Dogan, F. Compositional Effect of Thin Electrode Functional Layers on the Performance of Solid Oxide Fuel Cells. *J. Fuel Cell Sci. Technol.* **2011**, *8*, 061002−061002−6.

(25) Kim, B. S.; Lee, J. S.; Sekino, T.; Choa, Y. H.; Niihara, K. Hydrogen Reduction Behavior of NiO Dispersoid during Processing of $Al_2O_3$/Ni Nanocomposites. *Scr. Mater.* **2001**, *44*, 2121−2125.

(26) Fouquet, D.; Muller, A. C.; Weber, A.; Ivers-Tiffee, E. Kinetics of Oxidation and Reduction of Ni/YSZ Cermets. *Ionics* **2003**, *9*, 103−108.

(27) Waldbillig, D.; Wood, A.; Ivey, D. G. Thermal Analysis of the Cyclic Reduction and Oxidation Behaviour of SOFC Anodes. *Solid State Ionics* **2005**, *176*, 847−859.

(28) Zhang, L.; Li, M.; Song, X.; Guo, T.; Zhu, S.; Ji, W.; Wang, H. Preparation of Half-Cell by Bi-Layer Wet Powder Spraying and Tape Casting for Anode-Supported SOFCs. *J. Alloys Compd.* **2014**, *586*, 10−15.

(29) Kuboon, S.; Hu, Y. H. Study of NiO−CoO and $Co_3O_4$−$Ni_3O_4$ Solid Solutions in Multiphase Ni−Co−O Systems. *Ind. Eng. Chem. Res.* **2011**, *50*, 2015−2020.

(30) Boskovic, S.; Stevanovic, M. Sintering of Cobalt-Doped Nickel-Oxide. *J. Mater. Sci.* **1975**, *10*, 25−31.

(31) Elumalai, P.; Vasan, H. N.; Verelst, M.; Lecante, P.; Carles, V.; Tailhades, P. Synthesis and Characterization of Sub-Micron Size Co−Ni Alloys Using Malonate as Precursor. *Mater. Res. Bull.* **2002**, *37*, 353−363.

(32) Vassen, R.; Simwonis, D.; Stover, D. Modelling of the Agglomeration of Ni-Particles in Anodes of Solid Oxide Fuel Cells. *J. Mater. Sci.* **2001**, *36*, 147−151.
(33) Frontera, P.; Macario, A.; Aloise, A.; Antonucci, P. L.; Giordano, G.; Nagy, J. B. Effect of Support Surface on Methane Dry-Reforming Catalyst Preparation. *Catal. Today* **2013**, *218*, 18−29.
(34) Perejon, A.; Sanchez-Jimenez, P. E.; Criado, J. M.; Perez-Maqueda, L. A. Kinetic Analysis of Complex Solid-State Reactions. A New Deconvolution Procedure. *J. Phys. Chem. B* **2011**, *115*, 1780−1791.
(35) Svoboda, R.; Malek, J. Applicability of Fraser−Suzuki Function in Kinetic Analysis of Complex Crystallization Processes. *J. Therm. Anal. Calorim.* **2013**, *111*, 1045−1056.
(36) Szekely, J.; Lin, C. I.; Sohn, H. Y. Structural Model for Gas−Solid Reactions with a Moving Boundary. 5. Experimental Study of Reduction of Porous Nickel-Oxide Pellets with Hydrogen. *Chem. Eng. Sci.* **1973**, *28*, 1975−1989.
(37) Szekely, J.; Evans, J. W. Structural Model for Gas−Solid Reactions Involving a Moving Boundary—Reduction of Nickel Oxide with Hydrogen. *J. Met.* **1970**, *22*, A47−48.
(38) Chatterjee, R.; Banerjee, S.; Banerjee, S.; Ghosh, D. Reduction of Nickel Oxide Powder and Pellet by Hydrogen. *Trans. Indian Inst. Met.* **2012**, *65*, 265−273.
(39) Richardson, J. T.; Scates, R. M.; Twigg, M. V. X-Ray Diffraction Study of the Hydrogen Reduction of NiO/alpha-$Al_2O_3$ Steam Reforming Catalysts. *Appl. Catal., A* **2004**, *267*, 35−46.
(40) Lee, J. S.; Kim, B. S. Synthesis and Related Kinetics of Nanocrystalline Ni by Hydrogen Reduction of NiO. *Mater. Trans.* **2001**, *42*, 1607−1612.
(41) Taylor, G. B.; Starkweather, H. W. Reduction of Metal Oxides by Hydrogen. *J. Am. Chem. Soc.* **1930**, *52*, 2314−2325.
(42) Nilsson, A.; Pettersson, L. G. M. Chemical Bonding on Surfaces Probed by X-Ray Emission Spectroscopy and Density Functional Theory. *Surf. Sci. Rep.* **2004**, *55*, 49−167.
(43) Brown, M.; Primdahl, S.; Mogensen, M. Structure/Performance Relations for Ni/Yttria-Stabilized Zirconia Anodes for Solid Oxide Fuel Cells. *J. Electrochem. Soc.* **2000**, *147*, 475−485.
(44) Huang, Q. A.; Hui, R.; Wang, B. W.; Zhang, H. J. A Review of AC Impedance Modeling and Validation in SOFC Diagnosis. *Electrochim. Acta* **2007**, *52*, 8144−8164.
(45) Nakajima, H.; Kitahara, T.; Konomi, T. Electrochemical Impedance Spectroscopy Analysis of an Anode-Supported Microtubular Solid Oxide Fuel Cell. *J. Electrochem. Soc.* **2010**, *157*, B1686−B1692.
(46) Park, Y. M.; Lee, H. J.; Bae, H. Y.; Ahn, J. S.; Kim, H. Effect of Anode Thickness on Impedance Response of Anode-Supported Solid Oxide Fuel Cells. *Int. J. Hydrogen Energy* **2012**, *37*, 4394−4400.
(47) Endler, C.; Leonide, A.; Weber, A.; Tietz, F.; Ivers-Tiffee, E. Time-Dependent Electrode Performance Changes in Intermediate Temperature Solid Oxide Fuel Cells. *J. Electrochem. Soc.* **2010**, *157*, B292−B298.
(48) Zhang, L.; Liu, F.; Brinkman, K.; Reifsnider, K. L.; Virkar, A. V. A Study of Gadolinia-Doped Ceria Electrolyte by Electrochemical Impedance Spectroscopy. *J. Power Sources* **2014**, *247*, 947−960.
(49) Leonide, A.; Sonn, V.; Weber, A.; Ivers-Tiffee, E. Evaluation and Modeling of the Cell Resistance in Anode-Supported Solid Oxide Fuel Cells. *J. Electrochem. Soc.* **2008**, *155*, B36−B41.
(50) Baek, S. W.; Bae, J. Anodic Behavior of 8Y(2)O(3)-ZrO(2)/NiO Cermet Using an Anode-Supported Electrode. *Int. J. Hydrogen Energy* **2011**, *36*, 689−705.
(51) Mizusaki, J.; Tagawa, H.; Saito, T.; Yamamura, T.; Kamitani, K.; Hirano, K.; Ehara, S.; Takagi, T.; Hikita, T.; Ippommatsu, M.; Nakagawa, S.; Hashimoto, K. Kinetic-Studies of the Reaction at the Nickel Pattern Electrode on YSZ in $H_2$−$H_2O$ Atmospheres. *Solid State Ionics* **1994**, *70*, 52−58.
(52) Yoon, K. J.; Zink, P.; Gopalan, S.; Pal, U. B. Polarization Measurements on Single-Step Co-Fired Solid Oxide Fuel Cells (SOFCs). *J. Power Sources* **2007**, *172*, 39−49.
(53) Bieberle, A.; Gauckler, L. J. State-Space Modeling of the Anodic SOFC System Ni, H(2)−H(2)O Vertical Bar YSZ. *Solid State Ionics* **2002**, *146*, 23−41.
(54) Vogler, M.; Bieberle-Hutter, A.; Gauckler, L.; Warnatz, J.; Bessler, W. G. Modelling Study of Surface Reactions, Diffusion, and Spillover at a Ni/YSZ Patterned Anode. *J. Electrochem. Soc.* **2009**, *156*, B663−B672.
(55) Dar, Y. R.; Vijay, P.; Tade, M. O.; Datta, R. Topological Analysis of Hydrogen Oxidation Reaction Kinetics at Ni/YSZ Anode of the Solid Oxide Fuel Cell. *J. Electroanal. Chem.* **2012**, *677*, 15−23.
(56) Kawada, T.; Sakai, N.; Yokokawa, H.; Dokiya, M.; Mori, M.; Iwata, T. Structure and Polarization Characteristics of Solid Oxide Fuel-Cell Anodes. *Solid State Ionics* **1990**, *40−1*, 402−406.
(57) Mizusaki, J.; Tagawa, H.; Saito, T.; Kamitani, K.; Yamamura, T.; Hirano, K.; Ehara, S.; Takagi, T.; Hikita, T.; Ippommatsu, M.; Nakagawa, S.; Hashimoto, K. Preparation of Nickel Pattern Electrodes on YSZ and Their Electrochemical Properties in $H_2$−$H_2O$ Atmospheres. *J. Electrochem. Soc.* **1994**, *141*, 2129−2134.
(58) Nakagawa, N.; Nakajima, K.; Sato, M.; Kato, K. Contribution of the Internal Active Three-Phase Zone of Ni-Zirconia Cermet Anodes on the Electrode Performance of SOFCs. *J. Electrochem. Soc.* **1999**, *146*, 1290−1295.
(59) Besenbacher, F.; Chorkendorff, I.; Clausen, B. S.; Hammer, B.; Molenbroek, A. M.; Norskov, J. K.; Stensgaard, I. Design of a Surface Alloy Catalyst for Steam Reforming. *Science* **1998**, *279*, 1913−1915.